

The First X-ray Polarization Observation of the Black Hole X-ray Binary 4U 1630–47 in the Steep Power Law State

NICOLE RODRIGUEZ CAVERO ¹ LORENZO MARRA ² HENRIC KRAWCZYNSKI ¹ MICHAL DOVČIAK ³
STEFANO BIANCHI ² JAMES F. STEINER ⁴ JIRI SVOBODA ³ FIAMMA CAPITANIO ⁵ GIORGIO MATT ²
MICHELA NEGRO ^{6,7,8} ADAM INGRAM ⁹ ALEXANDRA VELEDINA ^{10,11} ROBERTO TAVERNA ¹² VLADIMIR KARAS ³
FRANCESCO URSINI ² JAKUB PODGORNÝ ^{13,3,14} AJAY RATHEESH ⁵ VALERY SULEIMANOV ¹⁵
ROMANA MIKUŠINCOVÁ ² SILVIA ZANE ¹⁶ PHILIP KAARET ¹⁷ FABIO MULERI ⁵ JURI POUTANEN ¹⁰
CHRISTIAN MALACARIA ¹⁸ PIERRE-OLIVIER PETRUCCI ¹⁹ EPHRAIM GAU ¹ KUN HU ¹ SOHEE CHUN ¹
IVÁN AGUDO ²⁰ LUCIO A. ANTONELLI ^{21,22} MATTEO BACHETTI ²³ LUCA BALDINI ^{24,25}
WAYNE H. BAUMGARTNER ¹⁷ RONALDO BELLAZZINI ²⁴ STEPHEN D. BONGIORNO ¹⁷ RAFFAELLA BONINO ^{26,27}
ALESSANDRO BREZ ²⁴ NICCOLÒ BUCCIANTINI ^{28,29,30} SIMONE CASTELLANO ²⁴ ELISABETTA CAVAZZUTI ³¹
CHIEN-TING CHEN ³² STEFANO CIPRINI ^{33,22} ENRICO COSTA ⁵ ALESSANDRA DE ROSA ⁵ ETTORE DEL MONTE ⁵
LAURA DI GESU ³¹ NICCOLÒ DI LALLA ³⁴ ALESSANDRO DI MARCO ⁵ IMMACOLATA DONNARUMMA ³¹
VICTOR DOROSHENKO ¹⁵ STEVEN R. EHLERT ¹⁷ TERUAKI ENOTO ³⁵ YURI EVANGELISTA ⁵ SERGIO FABIANI ⁵
RICCARDO FERRAZZOLI ⁵ JAVIER A. GARCÍA ³⁶ SHUICHI GUNJI ³⁷ KIYOSHI HAYASHIDA ^{38,*} JEREMY HEYL ³⁹
WATARU IWAKIRI ⁴⁰ SVETLANA G. JORSTAD ^{41,42} FABIAN KISLAT ⁴³ TAKAO KITAGUCHI ³⁵
JEFFERY J. KOLODZIEJCZAK ¹⁷ FABIO LA MONACA ⁵ LUCA LATRONICO ²⁶ IOANNIS LIODAKIS ⁴⁴
SIMONE MALDERA ²⁶ ALBERTO MANFREDA ⁴⁵ FRÉDÉRIC MARIN ⁴⁶ ANDREA MARINUCCI ³¹
ALAN P. MARSCHER ⁴¹ HERMAN L. MARSHALL ⁴⁷ FRANCESCO MASSARO ^{26,27} IKUYUKI MITSUISHI ⁴⁸
TSUNEFUMI MIZUNO ⁴⁹ CHI-YUNG NG ⁵⁰ STEPHEN L. O'DELL ¹⁷ NICOLA OMODEI ³⁴ CHIARA OPPEDISANO ²⁶
ALESSANDRO PAPITTO ²¹ GEORGE G. PAVLOV ⁵¹ ABEL L. PEIRSON ³⁴ MATTEO PERRI ^{22,21}
MELISSA PESCE-ROLLINS ²⁴ MAURA PILIA ²³ ANDREA POSSENTI ²³ SIMONETTA PUCCHETTI ²²
BRIAN D. RAMSEY ¹⁷ JOHN RANKIN ⁵ OLIVER J. ROBERTS ³² ROGER W. ROMANI ³⁴ CARMELO SGRÒ ²⁴
PATRICK SLANE ⁴ GLORIA SPANDRE ²⁴ PAOLO SOFFITTA ⁵ DOUGLAS A. SWARTZ ³² TORU TAMAGAWA ³⁵
FABRIZIO TAVECCHIO ⁵² YUZURU TAWARA ⁴⁸ ALLYN F. TENNANT ¹⁷ NICHOLAS E. THOMAS ¹⁷
FRANCESCO TOMBESI ^{53,33} ALESSIO TROIS ²³ SERGEY S. TSYGANKOV ¹⁰ ROBERTO TUROLLA ^{12,16}
JACCO VINK ⁵⁴ MARTIN C. WEISSKOPF ¹⁷ KINWAH WU ¹⁶ AND FEI XIE ^{55,5}

¹Physics Department, McDonnell Center for the Space Sciences, and Center for Quantum Leaps, Washington University in St. Louis, St. Louis, MO 63130, USA

²Dipartimento di Matematica e Fisica, Università degli Studi Roma Tre, Via della Vasca Navale 84, 00146 Roma, Italy

³Astronomical Institute of the Czech Academy of Sciences, Boční II 1401/1, 14100 Praha 4, Czech Republic

⁴Center for Astrophysics, Harvard & Smithsonian, 60 Garden St, Cambridge, MA 02138, USA

⁵INAF Istituto di Astrofisica e Planetologia Spaziali, Via del Fosso del Cavaliere 100, 00133 Roma, Italy

⁶University of Maryland, Baltimore County, Baltimore, MD 21250, USA

⁷NASA Goddard Space Flight Center, Greenbelt, MD 20771, USA

⁸Center for Research and Exploration in Space Science and Technology, NASA/GSFC, Greenbelt, MD 20771, USA

⁹School of Mathematics, Statistics, and Physics, Newcastle University, Newcastle upon Tyne NE1 7RU, UK

¹⁰Department of Physics and Astronomy, 20014 University of Turku, Finland

¹¹Nordita, KTH Royal Institute of Technology and Stockholm University, Hannes Alfvéns väg 12, SE-10691 Stockholm, Sweden

¹²Dipartimento di Fisica e Astronomia, Università degli Studi di Padova, Via Marzolo 8, 35131 Padova, Italy

¹³Université de Strasbourg, CNRS, Observatoire Astronomique de Strasbourg, UMR 7550, 67000 Strasbourg, France

¹⁴Astronomical Institute, Charles University, V Holešovičkách 2, CZ-18000, Prague, Czech Republic

¹⁵Institut für Astronomie und Astrophysik, Universität Tübingen, Sand 1, 72076 Tübingen, Germany

¹⁶Mullard Space Science Laboratory, University College London, Holmbury St Mary, Dorking, Surrey RH5 6NT, UK

¹⁷NASA Marshall Space Flight Center, Huntsville, AL 35812, USA

¹⁸International Space Science Institute (ISSI), Hallerstrasse 6, 3012, Bern, Switzerland

¹⁹Université Grenoble Alpes, CNRS, IPAG, 38000 Grenoble, France

²⁰Instituto de Astrofísica de Andalucía—CSIC, Glorieta de la Astronomía s/n, 18008 Granada, Spain

²¹INAF Osservatorio Astronomico di Roma, Via Frascati 33, 00078 Monte Porzio Catone (RM), Italy

²²Space Science Data Center, Agenzia Spaziale Italiana, Via del Politecnico snc, 00133 Roma, Italy

²³INAF Osservatorio Astronomico di Cagliari, Via della Scienza 5, 09047 Selargius (CA), Italy

- ²⁴*Istituto Nazionale di Fisica Nucleare, Sezione di Pisa, Largo B. Pontecorvo 3, 56127 Pisa, Italy*
- ²⁵*Dipartimento di Fisica, Università di Pisa, Largo B. Pontecorvo 3, 56127 Pisa, Italy*
- ²⁶*Istituto Nazionale di Fisica Nucleare, Sezione di Torino, Via Pietro Giuria 1, 10125 Torino, Italy*
- ²⁷*Dipartimento di Fisica, Università degli Studi di Torino, Via Pietro Giuria 1, 10125 Torino, Italy*
- ²⁸*INAF Osservatorio Astrofisico di Arcetri, Largo Enrico Fermi 5, 50125 Firenze, Italy*
- ²⁹*Dipartimento di Fisica e Astronomia, Università degli Studi di Firenze, Via Sansone 1, 50019 Sesto Fiorentino (FI), Italy*
- ³⁰*Istituto Nazionale di Fisica Nucleare, Sezione di Firenze, Via Sansone 1, 50019 Sesto Fiorentino (FI), Italy*
- ³¹*ASI - Agenzia Spaziale Italiana, Via del Politecnico snc, 00133 Roma, Italy*
- ³²*Science and Technology Institute, Universities Space Research Association, Huntsville, AL 35805, USA*
- ³³*Istituto Nazionale di Fisica Nucleare, Sezione di Roma “Tor Vergata”, Via della Ricerca Scientifica 1, 00133 Roma, Italy*
- ³⁴*Department of Physics and Kavli Institute for Particle Astrophysics and Cosmology, Stanford University, Stanford, California 94305, USA*
- ³⁵*RIKEN Cluster for Pioneering Research, 2-1 Hirosawa, Wako, Saitama 351-0198, Japan*
- ³⁶*California Institute of Technology, Pasadena, CA 91125, USA*
- ³⁷*Yamagata University, 1-4-12 Kojirakawa-machi, Yamagata-shi 990-8560, Japan*
- ³⁸*Osaka University, 1-1 Yamadaoka, Suita, Osaka 565-0871, Japan*
- ³⁹*University of British Columbia, Vancouver, BC V6T 1Z4, Canada*
- ⁴⁰*International Center for Hadron Astrophysics, Chiba University, Chiba 263-8522, Japan*
- ⁴¹*Institute for Astrophysical Research, Boston University, 725 Commonwealth Avenue, Boston, MA 02215, USA*
- ⁴²*Department of Astrophysics, St. Petersburg State University, Universitetsky pr. 28, Petrodvoretz, 198504 St. Petersburg, Russia*
- ⁴³*Department of Physics and Astronomy and Space Science Center, University of New Hampshire, Durham, NH 03824, USA*
- ⁴⁴*Finnish Centre for Astronomy with ESO, 20014 University of Turku, Finland*
- ⁴⁵*Istituto Nazionale di Fisica Nucleare, Sezione di Napoli, Strada Comunale Cinthia, 80126 Napoli, Italy*
- ⁴⁶*Université de Strasbourg, CNRS, Observatoire Astronomique de Strasbourg, UMR 7550, 67000 Strasbourg, France*
- ⁴⁷*MIT Kavli Institute for Astrophysics and Space Research, Massachusetts Institute of Technology, 77 Massachusetts Avenue, Cambridge, MA 02139, USA*
- ⁴⁸*Graduate School of Science, Division of Particle and Astrophysical Science, Nagoya University, Furo-cho, Chikusa-ku, Nagoya, Aichi 464-8602, Japan*
- ⁴⁹*Hiroshima Astrophysical Science Center, Hiroshima University, 1-3-1 Kagamiyama, Higashi-Hiroshima, Hiroshima 739-8526, Japan*
- ⁵⁰*Department of Physics, The University of Hong Kong, Pokfulam, Hong Kong*
- ⁵¹*Department of Astronomy and Astrophysics, Pennsylvania State University, University Park, PA 16802, USA*
- ⁵²*INAF Osservatorio Astronomico di Brera, Via E. Bianchi 46, 23807 Merate (LC), Italy*
- ⁵³*Dipartimento di Fisica, Università degli Studi di Roma “Tor Vergata”, Via della Ricerca Scientifica 1, 00133 Roma, Italy*
- ⁵⁴*Anton Pannekoek Institute for Astronomy & GRAPPA, University of Amsterdam, Science Park 904, 1098 XH Amsterdam, The Netherlands*
- ⁵⁵*Guangxi Key Laboratory for Relativistic Astrophysics, School of Physical Science and Technology, Guangxi University, Nanning 530004, China*

ABSTRACT

The *Imaging X-ray Polarimetry Explorer (IXPE)* observed the black hole X-ray binary 4U 1630–47 in the steep power law (or very high) state. The observations reveal a linear polarization degree of the 2–8 keV X-rays of $6.8 \pm 0.2\%$ at a position angle of $21^\circ 3' \pm 0^\circ 9'$ East of North (all errors at 1σ confidence level). Whereas the polarization degree increases with energy, the polarization angle stays constant within the accuracy of our measurements. We compare the polarization of the source in the steep power-law state with the previous *IXPE* measurement of the source in the high soft state. We find that even though the source flux and spectral shape are significantly different between the high soft state and the steep power-law state, their polarization signatures are similar. Assuming that the polarization of both the thermal and power-law emission components are constant over time, we estimate the power-law component polarization to be 6.8–7.0% and note that the polarization angle of the thermal and power-law components must be approximately aligned. We discuss the implications for the origin of the power-law component and the properties of the emitting plasma.

Keywords: Polarimetry (1278) — X-ray astronomy (1810) — Stellar mass black holes (1611)

1. INTRODUCTION

Black hole X-ray binaries (BHXRBS) harbor a stellar mass black hole in close orbit with a companion star. The matter accreting onto the central black hole forms an accretion disk which is heated by internal frictions to the point of emitting radiation that typically peaks in the X-ray band. BHXRBS sources are found in different spectral states. The two main states, the high soft and low hard states (HSS and LHS, respectively), exhibit a spectrum that can be roughly described as a combination of both a soft thermal component and a harder electron-scattering component with reflection by a cold medium. In the HSS, the X-rays are dominated by the thermal accretion disk emission followed by a non-thermal tail extending beyond 500 keV. This state is often fitted with a multi-temperature blackbody model and a power law $\propto E^{-\Gamma}$ with a photon index of $\Gamma \sim 2 - 2.2$ (Zdziarski & Gierliński 2004). In the LHS, the X-ray emission is dominated instead by photons that Compton scatter in a hot coronal plasma, though a low-temperature disk component can still be detected (McClintock & Remillard 2006). In this state, BHXRBS spectra consist of a cutoff power-law component with a typical photon index of $1.5 \leq \Gamma \leq 2.0$ and an exponential cutoff at high (~ 100 keV) energies as well as reflected emission from the corona off the disk (George & Fabian 1991; Done et al. 2007). BHXRBS can also be found in the steep power law (SPL) or very high state. The SPL state is characterized by competing thermal and power-law components—where the power-law component has a photon index of $\Gamma > 2.4$ (steeper than the higher energy tail of the HSS and the $\Gamma \sim 1.7$ detected in the LHS) (Remillard & McClintock 2006).

The *Imaging X-ray Polarimetry Explorer* (*IXPE*, Weisskopf et al. 2022) is a space-based observatory launched on 2021 December 9. *IXPE* has measured the linear polarization of the 2–8 keV X-rays from several BHXRBS, giving new insights into the configuration and properties of their emitting plasmas. The *IXPE* observations of the BHXRBS Cyg X-1 in the LHS revealed a 4% polarization aligned with the black hole radio jet, supporting the hypothesis that the jet might be launched from the black hole inner X-ray emitting region (Krawczynski et al. 2022). These results also revealed that the hot coronal plasma is extended parallel to the accretion disk plane and is seen at a higher inclination than the binary. *IXPE* observed a high polarization degree of $\sim 20\%$ perpendicular to radio ejections of the black hole candidate Cyg X-3 suggesting that the primary source is inherently highly luminous but obscured so that only the reflected emission can be observed (Veledina et al. 2023). The *IXPE* observations of the low-inclination high-mass BHXRBS LMC X-1 in the HSS gave only an upper limit on the total polarization degree of $< 2.2\%$ (Podgorny et al. 2023) for a combination of two main spectral components: dominant thermal emission with a modest contribution of Comptonization.

Observations of the transient low-mass X-ray binary (LMXRBS) 4U 1630–47 with the *Uhuru* satellite were first reported in Forman et al. (1976) and Jones et al. (1976), describing four outbursts occurring every ~ 600 days. The X-ray spectral and timing properties of the LMXRB during an outburst in 1984 suggest the compact object of 4U 1630–47 is a black hole candidate (Parmar et al. 1986) albeit with unusual outburst behavior (Chatterjee et al. 2022) indicative of a more complex system. The source spectrum tends to show strong, blueshifted absorption lines corresponding to Fe XXV and Fe XXVI transitions during the soft accretion states (Pahari et al. 2018; Gattuzz et al. 2019). Previous measurements of the 4U 1630–47 dust-scattering halo were used to estimate a distance range of 4.7–11.5 kpc (Kalemci et al. 2018). From the detection of short-duration dips in its X-ray light curve during outburst, a relatively high inclination of 60° – 75° has been inferred (Kuulkers et al. 1998). Various reflection spectral modeling efforts have consistently measured a high spin: $a = 0.985_{-0.014}^{+0.005}$ (King et al. 2014), $a = 0.92 \pm 0.04$ (Pahari et al. 2018), and $a \gtrsim 0.9$ (Connors et al. 2021).

IXPE previously observed 4U 1630–47 in the HSS where the detected emission was primarily from the thermal accretion disk (Ratheesh et al. 2023, henceforth Paper I). That observation revealed that the polarization degree increased with energy from $\sim 6\%$ at 2 keV to $\sim 10\%$ at 8 keV. The high polarization degree and its energy dependence cannot be explained in terms of a standard geometrically thin accretion disk with a highly or fully ionized accretion disk atmosphere (Chandrasekhar 1960; Sobolev 1949, 1963). While a standard thin disk viewed at inclinations $\gtrsim 85^\circ$ would produce a sufficiently high energy-integrated polarization degree, relativistic effects would lead to a decrease of the polarization degree with energy contrary to the observed increase. Such a high inclination would also lead to eclipsing of the source which has not been detected. In Paper I we argue that a geometrically thin disk with a partially ionized, outflowing emitting plasma can explain the observations. The absorption in the emitting plasma leads to escaping emission that is likelier to have scattered only once and ends up being highly polarized parallel to the

* Deceased

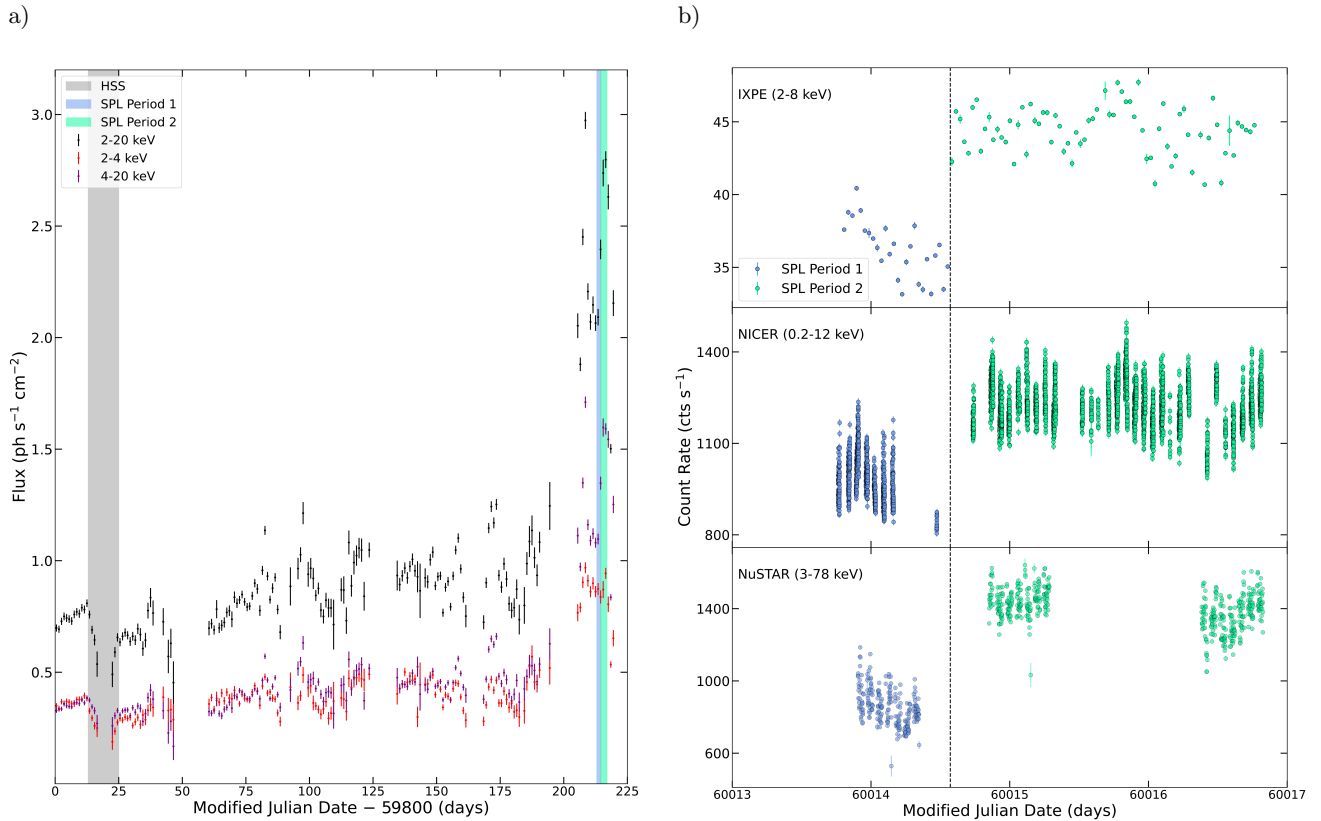


Figure 1. X-ray light curves of 4U 1630–47. a) MAXI light curve between MJD 59800 (2022 August 9) and MJD 60025 (2023 March 22). The flux in the 2–20, 2–4 and 4–20 keV energy bands are reported in black, orange, and purple, respectively. The gray-shaded region corresponds to the observation reported in Paper I when the source was in the HSS while the regions shaded in blue (Period 1) and green (Period 2) correspond to the observation reported in this paper when the source was in the SPL state. b) From top to bottom: *IXPE*, *NICER*, and *NuSTAR* light curves from March 10 to March 14, 2023. Observations of Periods 1 and 2 are shown by the blue and green data points, respectively, with a sudden flux increase at around MJD 60014.57 indicated by the vertical dashed line.

disk surface (Loskutov & Sobolev 1979, 1981; Taverna et al. 2021). A vertically outflowing emitting plasma leads to increased emission angles in the local disk frame due to relativistic aberration resulting in a higher polarization degree (e.g. Beloborodov 1998; Poutanen et al. 2023). Including absorption effects and the relativistic motion in the models achieves proper fits of the data for a thin accretion disk of a slowly spinning ($a \leq 0.5$) black hole seen at inclination $i \approx 75^\circ$ when the emitting plasma has an optical thickness of $\tau \sim 7$ and moves with a vertical velocity $v \sim 0.5 c$.

In this letter, we report on the first measurement of the polarization properties of a BHXR in the SPL state. The letter is organized as follows. We describe the *IXPE*, *NICER*, and *NuSTAR* observational results of 4U 1630–47 in Section 2 and present a comparison of the polarization of the source in the HSS and the SPL states. In Section 3, we examine our results in the context of previous *IXPE* X-ray polarization measurements of BHXR and discuss scenarios that could explain the observed polarization signature.

2. DATA SETS, ANALYSIS METHODS, AND RESULTS

IXPE performed a target of opportunity (ToO) observation of 4U 1630–47 between 2023 March 10 and 14 for ~ 150 ks after daily monitoring of the source by the Gas Slit Camera (GSC) on the Monitor of All-sky X-ray Image (MAXI) (Matsuoka et al. 2009) reported a significant increase in flux, as shown in Figure 1a. The MAXI flux was about $0.62 \text{ ph s}^{-1} \text{ cm}^{-2}$ during the gray highlighted region of the figure which coincides with the Paper I observation—hereby referred to as the HSS data. The blue and green highlighted regions have a higher flux of approximately $2.24 \text{ ph s}^{-1} \text{ cm}^{-2}$ and $2.77 \text{ ph s}^{-1} \text{ cm}^{-2}$, respectively, signaling a change in the emission state of the source. During these later time intervals, the 4–20 keV flux shown in purple in Figure 1a increases more drastically than the 2–4 keV

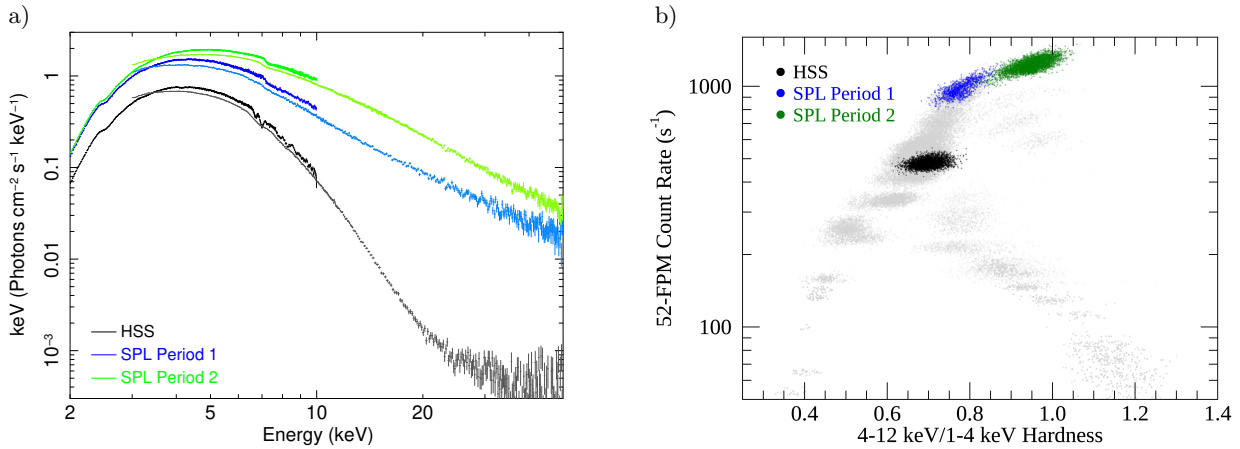


Figure 2. a) NICER (2–10 keV) and *NuSTAR* (3–50 keV) spectra of the HSS (black) from Paper I and from the current SPL Period 1 (blue) and Period 2 observations (green). The spectra were unfolded using a unit constant model for both instruments. b) Hardness-intensity diagram from NICER data of the HSS (black) and SPL state Period 1 (blue) and Period 2 (green), in 8 s intervals. Data from all previous NICER observations of 4U 1630–47 are shown in gray. Rates have been normalized as if all 52 of NICER’s FPMs were pointing at the source.

flux shown in orange indicating an increase in the spectral hardness over this time. Figure 1b shows the *IXPE*, NICER (Gendreau et al. 2012), and *NuSTAR* (Harrison et al. 2013) 2–8, 0.2–12, and 3–78 keV count rates during these later intervals. We see the source flux increased dramatically around the time marked in the figure by the vertical dashed line: the *IXPE*, NICER, and *NuSTAR* count rates increased by $\sim 23\%$, $\sim 25\%$, and $\sim 63\%$, respectively. The blanket *IXPE* coverage reveals that this increase was very sudden (about ~ 2.6 ks). Owing to the drastic change, we divided our *IXPE*, NICER, and *NuSTAR* observations into Period 1 (blue) to Period 2 (green) before and after 13:42:53 UTC on 2023 March 11. For a description of the *IXPE*, NICER, and *NuSTAR* data reduction, see Appendix A.

A comparison of the NICER and *NuSTAR* spectra in Figure 2a for the HSS observation (black) and Periods 1 and 2 (blue and green) reveals that the source transitioned from the HSS to the SPL state. In Paper I, the power-law component of the spectra contributed $\sim 3\%$ of the energy flux in the *IXPE* energy band. In contrast, our spectral fitting (see Appendix B) reveals that in Period 1 of the SPL state the power-law emission contributed $\sim 17\text{--}46\%$ of the 2–8 keV emission while in Period 2 this contribution increased to $\sim 40\text{--}92\%$. The soft HSS spectra are almost completely thermal in the form of a multi-temperature black body while the SPL spectra show an additional steep power-law component. From Figure 2a, we can see the SPL state shows an increase in 2–50 keV flux and a change in the spectral shape at energies above 5 keV. Only the HSS spectra exhibit prominent blueshifted Fe XXV and Fe XXVI lines as previously seen in past outbursts and explained in terms of over-ionization of the wind (Díaz Trigo et al. 2014) or of an intrinsic change of the physical properties of the wind itself (Hori et al. 2014) in the SPL state. Figure 2b shows a hardness–intensity diagram (HID) of 4U 1630–47 NICER data including the HSS (black) and SPL (blue and green) observations contemporaneous with the *IXPE* measurements, and archival data. Period 2 exhibits the highest rate corresponding to the largest relative contribution of the power-law flux. The energy flux in the 1–12 keV band increases with hardness during the transition from the HSS to the SPL state saturating at $\sim 1496 \text{ s}^{-1}$. Most astrophysical black hole candidates move through a hardness-intensity diagram counter-clockwise during outbursts (see Figure 7 of Fender et al. 2004 and Figure 1 of Homan & Belloni 2005). However, Figure 2b shows 4U 1630–47 evolving in a clockwise direction near the apex of the HID consistent with previous *Suzaku* observations of the source in the SPL state (Hori et al. 2014). We note that the variable motion of the source along the HID (see Figure 11 of Tomsick et al. 2005) makes it unclear if the source transitions from the HSS to the LHS through a high-intensity SPL regime or if we caught the source in an unusual pattern of motion. Furthermore, Figure 2b shows no evident bright hard state, consistent with the results of Capitanio et al. (2015) which could indicate a deviation from the standard HID Q-track shape proposed in Fender et al. (2004). Alternatively, Tomsick et al. (2014) suggest that a low large-scale magnetic field in the disk could delay the transition to the LHS.

During the entire SPL state observation, *IXPE* measured an energy-averaged 2–8 keV linear polarization degree (PD) of $6.8 \pm 0.2\%$ at a polarization angle (PA) 21.3 ± 0.9 (East of North) with a statistical confidence of over 30σ . The SPL state observation has a 1.5% smaller PD than the $8.32 \pm 0.17\%$ HSS PD reported in Paper I at a PA 3.5 higher

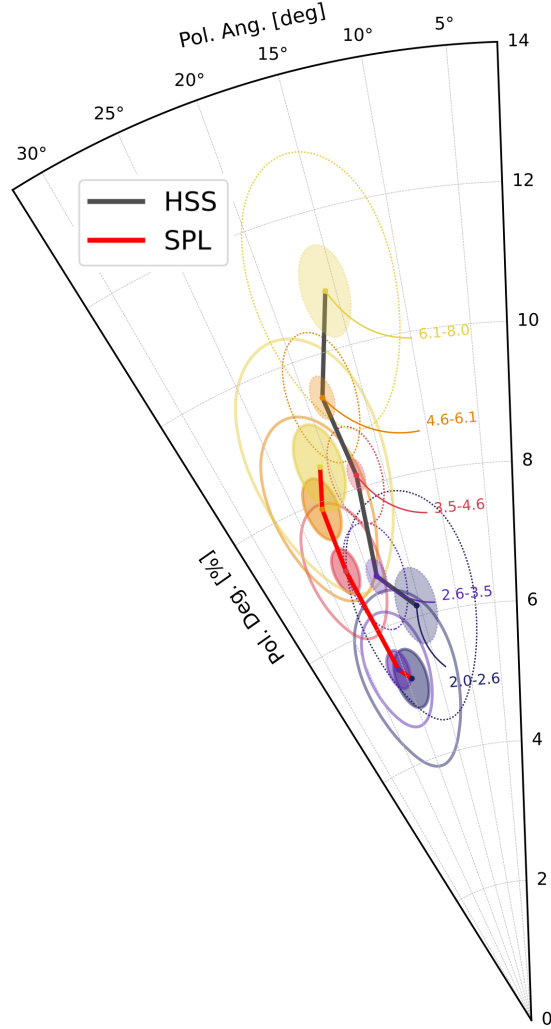


Figure 3. Measured PD and PA of 4U 1630–47 in 5 logarithmic energy bins: 2.0–2.6, 2.6–3.5, 3.5–4.6, 4.6–6.1, and 6.1–8.0 keV. The black line and transparent contours show the polarization in the HSS reported in Paper I. The red solid line and solid contours show the polarization in the SPL state (this paper). The shaded and unshaded ellipses show their 68.3% and 99.7% confidence regions, respectively. Errors on PD and PA computed by IXPEOBSSIM are derived from the Q and U gaussian errors according to the formalism developed by Kislak et al. (2015).

with respect to the previously observed $17^{\circ}8 \pm 0^{\circ}6$. Figure 3 shows the time-averaged polarization signature during both states in 5 logarithmic energy bands. The PA is constant within 3σ during the HSS and SPL observations. The summary of measured PD and PA in different spectral states is given in Table 1. These values have been computed using the PCUBE algorithm of the IXPEOBSSIM analysis software (Baldini et al. 2022). Figure 4 shows linear and constant fits of PD and PA, respectively, obtained using XSPEC (Arnaud 1996). The HSS and SPL state observations have a similar linear dependence of the PD on the photon energy E , with a linear model $\text{PD} = p_0 + \alpha(E/1 \text{ keV})$. For the HSS, the reported values are $p_0 = 3.47 \pm 0.54\%$, $\alpha = 1.12 \pm 0.13\%$ with the null hypothesis probability of 3.55×10^{-16} for a constant function. For the SPL state Period 1 observation, these parameters change to $p_0 = 2.7 \pm 1.3\%$, $\alpha = 1.08 \pm 0.32\%$ with the null hypothesis probability of 1.42×10^{-2} for a constant function. For the SPL state Period 2 observation, these parameters are $p_0 = 2.44 \pm 0.70\%$, $\alpha = 0.88 \pm 0.16\%$ with the null hypothesis probability of 4.56×10^{-7} for a constant function. Both the HSS and SPL Period 1 and Period 2 observations show relatively energy-independent PA in the IXPE band, with the fitted value of PA being $18^{\circ}0 \pm 0^{\circ}5$, $21^{\circ}4 \pm 1^{\circ}8$ and $21^{\circ}5 \pm 0^{\circ}9$ with the null hypothesis probability of 0.607, 0.854 and 0.877, respectively.

Table 1. Polarization properties in different spectral states of 4U 1630–47. The estimated fractions of the thermal and power-law flux contributing to the 2–8 keV energy band are also given.

Spectral state	Polarization degree	Polarization angle	Thermal contribution		Power-law contribution	
	[%]	[deg]	Fit 1	Fit 2	Fit 1	Fit 2
HSS	8.32 ± 0.17	17.8 ± 0.6		0.97		0.03
SPL Period 1	7.55 ± 0.44	21.7 ± 1.7	0.54	0.83	0.46	0.17
SPL Period 2	6.52 ± 0.24	21.3 ± 1.1	0.08	0.60	0.92	0.40
SPL Total	6.75 ± 0.21	21.3 ± 0.9		–		–

NOTE—Flux contributions are parameter-dependent. See Appendix B for more details on the model used. Contributions are calculated using either disk blackbody seed radiation (Fit 1) or blackbody seed radiation (Fit 2) for the power-law component of the spectra in the SPL Period 1 and 2 cases.

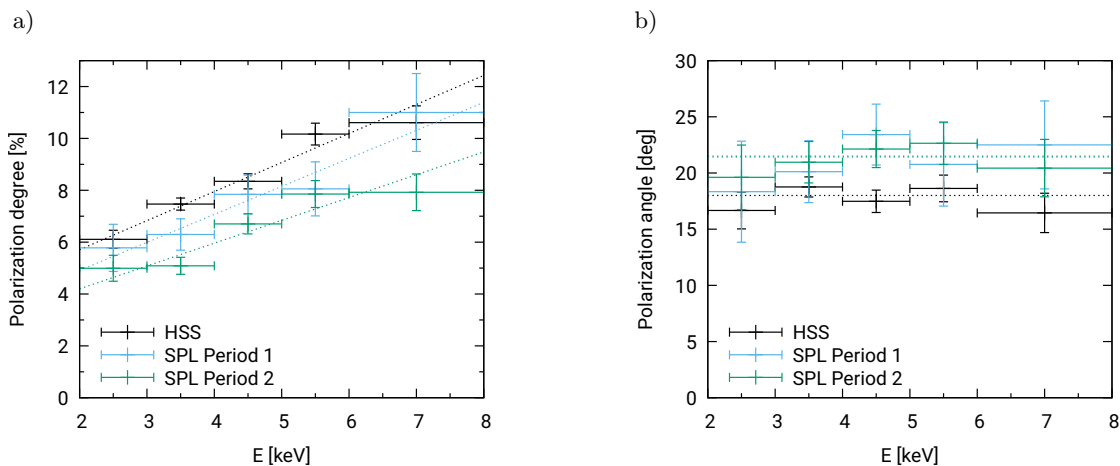


Figure 4. a) PD and b) PA as a function of energy in the *IXPE* 2–8 keV energy range. Comparison of the 4U 1630–47 polarization properties in the HSS (black), reported in Paper I, and in the SPL Period 1 (blue) and Period 2 (green) discussed in this paper. Linear fits for PD and constant fit for PA are also shown in dotted lines (see the text for the fit details).

To study the polarization properties of the power-law component, we performed a polarimetric fit of the data starting from the spectral analysis described in Appendix B. We included the *IXPE* *Q* and *U* spectra in the spectral fit and convolved the thermal and power-law spectral components with two `pollin` models¹. This allowed us to attribute polarization to each component separately assuming that the PD depends linearly on the photon energy E : $PD = p_0 + \alpha(E/1 \text{ keV})$. In Paper I, we found that the only spectral component contributing significantly to the HSS emission is the thermal one. We assumed that the polarization of this thermal component remains constant between the HSS and SPL states requiring that $p_{0\text{Thermal}} = 3.47\%$ and $\alpha_{\text{Thermal}} = 1.12\%$ as per the HSS fit shown in Figure 4a. Due to the relatively constant PA during the HSS, SPL Period 1, and SPL Period 2 observations (Figure 4b), we further assumed that the thermal and non-thermal components have equal PA and allowed it to vary between SPL periods. Additionally, the PA appears to be energy-independent so our fits take the PA to be constant with energy: $PA = \psi$. As shown in Table 1, the estimates of the power-law component flux contribution depend on the model parameters used and will therefore also affect the estimate of the polarization properties of the power-law component. Figure 5 summarizes the results of our linear fits for the non-thermal component PD resulting from Fits 1 and 2 as well as the assumed thermal component PD for comparison. For Fit 1, we assumed a multi-color blackbody as the Comptonized component input radiation (Figure 6a). For the PD of the power-law component, we found that $\alpha_{\text{Fit1}} = 1.05 \pm 0.45\%$

¹ For a description of the linearly dependent polarization model see <https://heasarc.gsfc.nasa.gov/xanadu/xspec/manual/node213.html>. Note that these equations have been modified to the form described in the text.

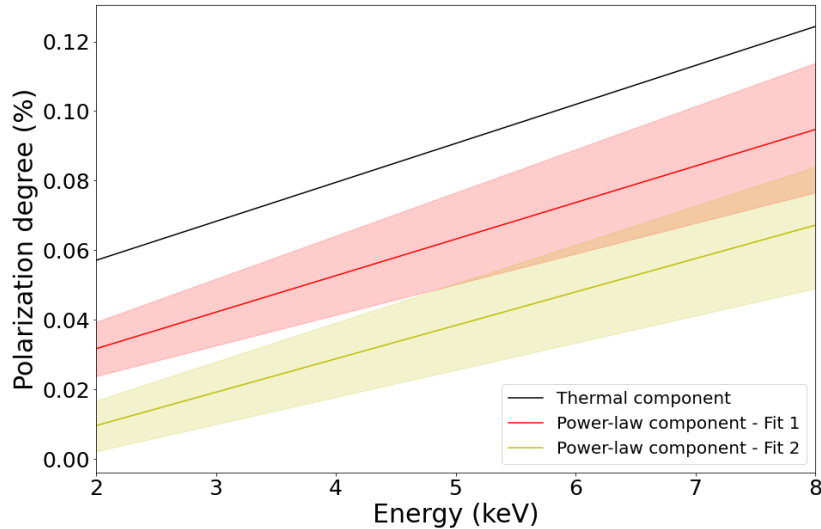


Figure 5. Best linear fits with respect to energy of thermal component (black), power-law component for Fit 1 (red), and power-law component for Fit 2 (yellow). The shaded regions show the 1σ confidence intervals.

and we set an upper limit on $p_{0\text{Fit1}}$ of 2.7%. The $p_{0\text{Fit1}}$ upper limit tells us that the Comptonization component could be unpolarized at 0 keV but this is just an extrapolation—the power-law PD in the 2–8 keV energy range (Figure 5) shows that the component is polarized. The computed PAs for Period 1 and Period 2 are $\psi_{\text{Fit1-P1}} = 21^\circ 0 \pm 3^\circ 4$ and $\psi_{\text{Fit1-P2}} = 21^\circ 7 \pm 2^\circ 2$. For Fit 2 (Figure 6b), we assume a simple blackbody as a seed for the power-law radiation. In this case, the thermal emission is the main source of flux in the 2–8 keV energy range for both Periods 1 and 2. The PD of the power-law component can be fitted with $\alpha_{\text{Fit2}} = 0.96 \pm 0.26\%$ and we were only able to set an upper limit on $p_{0\text{Fit2}}$ of 1.3%. The corresponding PAs for Period 1 and Period 2 are $\psi_{\text{Fit2-P1}} = 21^\circ 0 \pm 3^\circ 5$ and $\psi_{\text{Fit2-P2}} = 21^\circ 7 \pm 2^\circ 1$. We also calculated the 2–8 keV average PD of the power-law component from the *IXPE* *I*, *Q*, and *U* fluxes. For Fit 1, we get $7.0 \pm 3.2\%$ and $6.8 \pm 2.6\%$ in Periods 1 and 2, respectively. For Fit 2, we get $6.8 \pm 3.9\%$ and $7.0 \pm 2.2\%$ in Periods 1 and 2, respectively.

3. DISCUSSION

IXPE observed 4U 1630–47 in the HSS (Paper I) and in the SPL state (this paper). We find that the HSS and SPL exhibit surprisingly similar polarization properties despite their very different energy spectra. Although the PD of the HSS (increasing from 6% to 10% between 2 to 8 keV) exceeded that of the SPL observations (increasing from 5% to 8% between 2 to 8 keV), and Figure 4a shows that the PD of Period 2 decreases with respect to Period 1, we note that the PD varied as much during the HSS observations (Fig. M3 of Paper I) as it did between the HSS and the SPL observations. The change in polarization direction $\sim 3^\circ 5$ is not statistically significant (3σ). While the HSS spectrum was dominated by the thermal component, our spectral analysis shows that the Comptonization component increased by a large factor between the HSS, SPL Period 1 and Period 2, although its exact flux contribution is model parameter-dependent. Since the polarization angle stays almost the same with vastly different flux contributions of the power-law component, this component has to be polarized in a similar direction as the thermal component. Our polarimetric analysis reveals that the power-law component has an energy-integrated PD of 6.8–7.0% in both cases analyzed, i.e. using either multicolor disk blackbody or single temperature blackbody as seed photons for Comptonization. Since both cases suggest substantially different contributions of this component to the total flux, we consider this estimate to be quite independent of the model assumptions. Note that the dominating thermal component in HSS had a PD of 8.3 %, thus the Comptonized component is slightly less polarized than the thermal one by approximately 1.3–1.5%.

This congruence of the PD and directions is puzzling if the emission comes from spatially distinct regions and is produced by different physical emission mechanisms. Direct thermal emission from the disk tends to be polarized parallel to the accretion disk except for close to the innermost stable circular orbit (ISCO) where strong gravitational

effects rotate the PA by about 10° (Connors & Stark 1977; Loktev et al. 2022). Gravitationally lensed photons that scatter off the disk (known as returning radiation) are polarized perpendicular to the direct thermal radiation (Schnittman & Krolik 2009). Comptonization, commonly invoked to explain the power-law component, gives rise to a polarization perpendicular to the spatial extent of the Comptonizing plasma (Poutanen & Svensson 1996; Schnittman & Krolik 2010; Krawczynski & Beheshtipour 2022). The apparent alignment of the polarization directions of the thermal and power-law emission could imply that the Comptonizing plasma of the SPL state is extended perpendicular to the accretion disk—contrary to what we inferred for the hard state of Cyg X-1 (Krawczynski et al. 2022). However, it is worth noting that for a slab corona geometry, polarization is parallel to the disk at photon energies where the first Compton scattering dominates the flux (Poutanen et al. 2023). Since the temperature of the disk is high ($kT_{\text{bb}} \approx 1.5$ keV), the first scattering could dominate in the *IXPE* energy range such that the PA of the disk and the up-scattered component are aligned.

Based on the *IXPE* results, we posit that the HSS and SPL states could exhibit similar disk geometries and involve similar emission processes. In the scenario discussed in Paper I, an outflowing, partially-ionized accretion disk atmosphere produces the observed high PD as a result of Thomson scattering. The electrons in the outflow attain Compton temperature (a few keV) if efficient heating and acceleration mechanisms, such as shocks, magnetic reconnection, and turbulence, do not operate. Instantaneous increase of electron heating and acceleration may lead to a change of the scattering mechanism—from Thomson to inverse Compton—producing the observed power-law component. During the transitions between the soft and hard states, the observed spectra are known to be well fitted with Comptonization from low-temperature thermal or hybrid (thermal and non-thermal) electrons (Gierliński et al. 1999; Zdziarski et al. 2001; Życki et al. 2001), with a typical temperature of the Maxwellian part ~ 10 keV. Increased electron temperature, in general, causes the reduction of the PD (e.g., Fig. 2 of Poutanen 1994); however for these low electron temperatures the effect is rather small and the polarization signatures remain similar to (albeit not exactly the same as in) the Thomson-scattering case. The observed variations of the PD during the HSS and SPL states could result from changes in the scattered fraction and/or the outflow velocities.

As mentioned in Paper I and in West & Krawczynski (2023), non-vanishing accretion disk geometrical thicknesses may play a role in explaining the high polarization fractions of the source. Spectral fitting indicates that the disk temperature kT_{bb} increased between the HSS (in Paper I) and the SPL state. This increase in temperature is expected if a thicker accretion disk is present in the SPL state (Tomsick et al. 2005). As higher energy photons originate closer to the black hole and are more likely to scatter, this scenario naturally explains PD increasing with photon energy. In contrast, the reflection off distant features (e.g. off a wind) would give rise to rather energy-independent PD. We also note that the neutral hydrogen column density is much smaller in the SPL than in the HSS state. The similar polarization properties of the emission from both states confirm our conclusion from Paper I that scattering off the wind is most likely not the dominant mechanism explaining the high polarization of the X-ray emission.

On the other hand, we note that spectral timing studies of black hole LMXRBs suggest that their coronae contract in the hard state and then expand during the hard-to-soft state transition (Wang et al. 2022). Soft reverberation lag modeling employing a lamppost corona estimates that the corona height increases by an order of magnitude during the state transition (Wang et al. 2021). If this increase in height were to be accompanied by a decrease in width, we could expect a change in the shape of the corona from laterally extended in the LHS to vertically extended—and hence giving rise to large reverberation lags—in the intermediate states. Our polarization results could then be explained by a cone or lamppost-shaped corona in the SPL state. Future polarization measurements of the source, particularly in the LHS, could help constrain the evolution of the corona geometry as well as the polarization of the power-law component.

In other alternative scenarios, the power-law component could originate as synchrotron emission from a jet perpendicular to the accretion disk threaded by a magnetic field aligned with the jet; or from synchrotron emission from non-thermal electrons accelerated in the plunging region, gyrating in a magnetic field perpendicular to the accretion disk (Hankla et al. 2022). This model would require just the right amount of magnetic field non-uniformity to explain the rather low PD of the power-law emission for synchrotron emission. Yan & Wang (2011) propose that the SPL state originates from synchrotron radiation of magnetized compact spots near the ISCO, down-scattered by thermal electrons in the corona. Also here, some fine-tuning is required so that the combined thermal and power-law emission end up having similar polarization signatures as the thermal emission alone.

1 *Acknowledgments:* The *IXPE* is a joint US and Italian mission. The US contribution is supported by NASA and led and
 2 managed by its Marshall Space Flight Center (MSFC), with industry partner Ball Aerospace (contract NNM15AA18C).
 3 The Italian contribution is supported by the Italian Space agency (Agenzia Spaziale Italiana, ASI) through contract
 4 ASI-OHBI-2017-12-I.0, agreements ASI-INAF-2017-12-H0 and ASI-INFN-2017.13-H0, and its Space Science Data
 5 Center (SSDC), and by the Istituto Nazionale di Astrofisica (INAF) and the Istituto Nazionale di Fisica Nucleare
 6 (INFN) in Italy. This research used data and software products or online services provided by the *IXPE* Team (Marshall
 7 Space Flight Center, the Space Science Data Center of the Italian Space Agency, the Istituto Nazionale di Astrofisica,
 8 and Istituto Nazionale di Fisica Nucleare), as well as the High-Energy Astrophysics Science Archive Research Center
 9 (HEASARC), at NASA Goddard Space Flight Center. N.R.C and H.K acknowledge NASA support through the
 10 grants NNX16AC42G, 80NSSC20K0329, 80NSSC20K0540, NAS8- 03060, 80NSSC21K1817, 80NSSC22K1291, and
 11 80NSSC22K1883 as well as support from the McDonnell Center for the Space Sciences. M.D., J.Sv., V.K. and J.Pod.
 12 acknowledge the support from the Czech Science Foundation project GACR 21-06825X and the institutional support
 13 from the Astronomical Institute of the Czech Academy of Sciences RVO:67985815. A.I. acknowledges support from the
 14 Royal Society. M.N. acknowledges the support by NASA under award number 80GSFC21M0002. POP acknowledges
 15 financial support from the French High Energy Programme (PNHE) of the CNRS as well as from the French Space
 16 Agency (CNES).

REFERENCES

- Arnaud, K. A. 1996, in ASP Conf. Ser., Vol. 101,
 Astronomical Data Analysis Software and Systems V, ed.
 G. H. Jacoby & J. Barnes (San Francisco: Astron. Soc.
 Pac.), 17–20
- Baldini, L., Bucciantini, N., Lalla, N. D., et al. 2022,
 SoftwareX, 19, 101194, doi: [10.1016/j.softx.2022.101194](https://doi.org/10.1016/j.softx.2022.101194)
- Beloborodov, A. M. 1998, ApJL, 496, L105,
 doi: [10.1086/311260](https://doi.org/10.1086/311260)
- Capitaniao, F., Campana, R., De Cesare, G., & Ferrigno, C.
 2015, MNRAS, 450, 3840, doi: [10.1093/mnras/stv687](https://doi.org/10.1093/mnras/stv687)
- Chandrasekhar, S. 1960, Radiative Transfer (New York:
 Dover Publications)
- Chatterjee, K., Debnath, D., Bhowmick, R., Nath, S. K., &
 Chatterjee, D. 2022, MNRAS, 510, 1128,
 doi: [10.1093/mnras/stab3570](https://doi.org/10.1093/mnras/stab3570)
- Connors, P. A., & Stark, R. F. 1977, Nature, 269, 128,
 doi: [10.1038/269128a0](https://doi.org/10.1038/269128a0)
- Connors, R. M. T., García, J. A., Tomsick, J., et al. 2021,
 ApJ, 909, 146, doi: [10.3847/1538-4357/abdd2c](https://doi.org/10.3847/1538-4357/abdd2c)
- Di Marco, A., Soffitta, P., Costa, E., et al. 2023, AJ, 165,
 143, doi: [10.3847/1538-3881/acba0f](https://doi.org/10.3847/1538-3881/acba0f)
- Díaz Trigo, M., Migliari, S., Miller-Jones, J. C. A., &
 Guainazzi, M. 2014, A&A, 571, A76,
 doi: [10.1051/0004-6361/201424554](https://doi.org/10.1051/0004-6361/201424554)
- Done, C., Gierliński, M., & Kubota, A. 2007, A&A Rv, 15,
 1, doi: [10.1007/s00159-007-0006-1](https://doi.org/10.1007/s00159-007-0006-1)
- Fender, R. P., Belloni, T. M., & Gallo, E. 2004, MNRAS,
 355, 1105, doi: [10.1111/j.1365-2966.2004.08384.x](https://doi.org/10.1111/j.1365-2966.2004.08384.x)
- Ferland, G. J., Chatzikos, M., Guzmán, F., et al. 2017,
 RMxAA, 53, 385, doi: [10.48550/arXiv.1705.10877](https://doi.org/10.48550/arXiv.1705.10877)
- Forman, W., Jones, C., & Tananbaum, H. 1976, ApJL, 207,
 L25, doi: [10.1086/182170](https://doi.org/10.1086/182170)
- Gatuzz, E., Díaz Trigo, M., Miller-Jones, J. C. A., &
 Migliari, S. 2019, MNRAS, 482, 2597,
 doi: [10.1093/mnras/sty2850](https://doi.org/10.1093/mnras/sty2850)
- Gendreau, K. C., Arzoumanian, Z., & Okajima, T. 2012, in
 Proc. SPIE, Vol. 8443, Space Telescopes and
 Instrumentation 2012: Ultraviolet to Gamma Ray, ed.
 T. Takahashi, S. S. Murray, & J.-W. A. den Herder,
 844313, doi: [10.1117/12.926396](https://doi.org/10.1117/12.926396)
- George, I. M., & Fabian, A. C. 1991, MNRAS, 249, 352,
 doi: [10.1093/mnras/249.2.352](https://doi.org/10.1093/mnras/249.2.352)
- Gierliński, M., Zdziarski, A. A., Poutanen, J., et al. 1999,
 MNRAS, 309, 496, doi: [10.1046/j.1365-8711.1999.02875.x](https://doi.org/10.1046/j.1365-8711.1999.02875.x)
- Hankla, A. M., Scepi, N., & Dexter, J. 2022, MNRAS, 515,
 775, doi: [10.1093/mnras/stac1785](https://doi.org/10.1093/mnras/stac1785)
- Harrison, F. A., Craig, W. W., Christensen, F. E., et al.
 2013, ApJ, 770, 103, doi: [10.1088/0004-637X/770/2/103](https://doi.org/10.1088/0004-637X/770/2/103)
- Homan, J., & Belloni, T. 2005, Ap&SS, 300, 107,
 doi: [10.1007/s10509-005-1197-4](https://doi.org/10.1007/s10509-005-1197-4)
- Hori, T., Ueda, Y., Shidatsu, M., et al. 2014, ApJ, 790, 20,
 doi: [10.1088/0004-637X/790/1/20](https://doi.org/10.1088/0004-637X/790/1/20)
- Jones, C., Forman, W., Tananbaum, H., & Turner, M. J. L.
 1976, ApJL, 210, L9, doi: [10.1086/182291](https://doi.org/10.1086/182291)
- Joye, W. A., & Mandel, E. 2003, in ASP Conf. Ser., Vol.
 295, Astronomical Data Analysis Software and Systems
 XII, ed. H. E. Payne, R. I. Jedrzejewski, & R. N. Hook
 (San Francisco: Astron. Soc. Pac.), 489
- Kalemci, E., Maccarone, T. J., & Tomsick, J. A. 2018, ApJ,
 859, 88, doi: [10.3847/1538-4357/aabcd3](https://doi.org/10.3847/1538-4357/aabcd3)

- King, A. L., Walton, D. J., Miller, J. M., et al. 2014, *ApJL*, 784, L2, doi: [10.1088/2041-8205/784/1/L2](https://doi.org/10.1088/2041-8205/784/1/L2)
- Kislat, F., Clark, B., Beilicke, M., & Krawczynski, H. 2015, *Astroparticle Physics*, 68, 45, doi: [10.1016/j.astropartphys.2015.02.007](https://doi.org/10.1016/j.astropartphys.2015.02.007)
- Krawczynski, H., & Beheshtipour, B. 2022, *ApJ*, 934, 4, doi: [10.3847/1538-4357/ac7725](https://doi.org/10.3847/1538-4357/ac7725)
- Krawczynski, H., Muleri, F., Dovčiak, M., et al. 2022, *Science*, 378, 650, doi: [10.1126/science.add5399](https://doi.org/10.1126/science.add5399)
- Kuulkers, E., Wijnands, R., Belloni, T., et al. 1998, *ApJ*, 494, 753, doi: [10.1086/305248](https://doi.org/10.1086/305248)
- Li, L.-X., Zimmerman, E. R., Narayan, R., & McClintock, J. E. 2005, *ApJS*, 157, 335, doi: [10.1086/428089](https://doi.org/10.1086/428089)
- Loktev, V., Veledina, A., & Poutanen, J. 2022, *A&A*, 660, A25, doi: [10.1051/0004-6361/202142360](https://doi.org/10.1051/0004-6361/202142360)
- Loskutov, V. M., & Sobolev, V. V. 1979, *Astrofizika*, 15, 241
- . 1981, *Astrofizika*, 17, 97
- Madsen, K. K., Forster, K., Grefenstette, B., Harrison, F. A., & Miyasaka, H. 2022, *Journal of Astronomical Telescopes, Instruments, and Systems*, 8, 034003, doi: [10.1117/1.JATIS.8.3.034003](https://doi.org/10.1117/1.JATIS.8.3.034003)
- Matsuoka, M., Kawasaki, K., Ueno, S., et al. 2009, *PASJ*, 61, 999, doi: [10.1093/pasj/61.5.999](https://doi.org/10.1093/pasj/61.5.999)
- McClintock, J. E., & Remillard, R. A. 2006, in *Compact stellar X-ray sources*, ed. W. Lewin & M. van der Klis (Cambridge: Cambridge University Press), 157–213, doi: [10.48550/arXiv.astro-ph/0306213](https://doi.org/10.48550/arXiv.astro-ph/0306213)
- Nasa High Energy Astrophysics Science Archive Research Center (Heasarc). 2014, HEASoft: Unified Release of FTOOLS and XANADU, Astrophysics Source Code Library, record ascl:1408.004. <http://ascl.net/1408.004>
- Pahari, M., Bhattacharyya, S., Rao, A. R., et al. 2018, *ApJ*, 867, 86, doi: [10.3847/1538-4357/aae53b](https://doi.org/10.3847/1538-4357/aae53b)
- Parmar, A. N., Stella, L., & White, N. E. 1986, *ApJ*, 304, 664, doi: [10.1086/164204](https://doi.org/10.1086/164204)
- Podgorny, J., Marra, L., Muleri, F., et al. 2023, arXiv e-prints, arXiv:2303.12034, doi: [10.48550/arXiv.2303.12034](https://doi.org/10.48550/arXiv.2303.12034)
- Poutanen, J. 1994, *ApJS*, 92, 607, doi: [10.1086/192024](https://doi.org/10.1086/192024)
- Poutanen, J., & Svensson, R. 1996, *ApJ*, 470, 249, doi: [10.1086/177865](https://doi.org/10.1086/177865)
- Poutanen, J., Veledina, A., & Beloborodov, A. M. 2023, *ApJL*, in press, arXiv:2302.11674, doi: [10.48550/arXiv.2302.11674](https://doi.org/10.48550/arXiv.2302.11674)
- Ratheesh, A., Dovčiak, M., Krawczynski, H., et al. 2023, *Nature Astronomy*, submitted, arXiv:2304.12752, doi: [10.48550/arXiv.2304.12752](https://doi.org/10.48550/arXiv.2304.12752)
- Remillard, R. A., & McClintock, J. E. 2006, *ARA&A*, 44, 49, doi: [10.1146/annurev.astro.44.051905.092532](https://doi.org/10.1146/annurev.astro.44.051905.092532)
- Schnittman, J. D., & Krolik, J. H. 2009, *ApJ*, 701, 1175, doi: [10.1088/0004-637X/701/2/1175](https://doi.org/10.1088/0004-637X/701/2/1175)
- . 2010, *ApJ*, 712, 908, doi: [10.1088/0004-637X/712/2/908](https://doi.org/10.1088/0004-637X/712/2/908)
- Sobolev, V. V. 1949, *Uch. Zap. Leningrad Univ.*, 16
- . 1963, *A treatise on radiative transfer* (Princeton: Van Nostrand)
- Taverna, R., Marra, L., Bianchi, S., et al. 2021, *MNRAS*, 501, 3393, doi: [10.1093/mnras/staa3859](https://doi.org/10.1093/mnras/staa3859)
- Tomsick, J. A., Corbel, S., Goldwurm, A., & Kaaret, P. 2005, *ApJ*, 630, 413, doi: [10.1086/431896](https://doi.org/10.1086/431896)
- Tomsick, J. A., Yamaoka, K., Corbel, S., et al. 2014, *ApJ*, 791, 70, doi: [10.1088/0004-637X/791/1/70](https://doi.org/10.1088/0004-637X/791/1/70)
- Veledina, A., Muleri, F., Poutanen, J., et al. 2023, arXiv e-prints, arXiv:2303.01174, doi: [10.48550/arXiv.2303.01174](https://doi.org/10.48550/arXiv.2303.01174)
- Wang, J., Mastroserio, G., Kara, E., et al. 2021, *ApJL*, 910, L3, doi: [10.3847/2041-8213/abec79](https://doi.org/10.3847/2041-8213/abec79)
- Wang, J., Kara, E., Lucchini, M., et al. 2022, *ApJ*, 930, 18, doi: [10.3847/1538-4357/ac6262](https://doi.org/10.3847/1538-4357/ac6262)
- Weisskopf, M. C., Soffitta, P., Baldini, L., et al. 2022, *Journal of Astronomical Telescopes, Instruments, and Systems*, 8, 026002, doi: [10.1117/1.JATIS.8.2.026002](https://doi.org/10.1117/1.JATIS.8.2.026002)
- West, A., & Krawczynski, H. 2023, *ApJ*
- Wilms, J., Allen, A., & McCray, R. 2000, *ApJ*, 542, 914, doi: [10.1086/317016](https://doi.org/10.1086/317016)
- Yan, L.-H., & Wang, J.-C. 2011, *Research in Astronomy and Astrophysics*, 11, 631, doi: [10.1088/1674-4527/11/6/002](https://doi.org/10.1088/1674-4527/11/6/002)
- Zdziarski, A. A., & Gierliński, M. 2004, *Progress of Theoretical Physics Supplement*, 155, 99, doi: [10.1143/PTPS.155.99](https://doi.org/10.1143/PTPS.155.99)
- Zdziarski, A. A., Grove, J. E., Poutanen, J., Rao, A. R., & Vadawale, S. V. 2001, *ApJL*, 554, L45, doi: [10.1086/320932](https://doi.org/10.1086/320932)
- Zdziarski, A. A., Johnson, W. N., & Magdziarz, P. 1996, *MNRAS*, 283, 193, doi: [10.1093/mnras/283.1.193](https://doi.org/10.1093/mnras/283.1.193)
- Życki, P. T., Done, C., & Smith, D. A. 1999, *MNRAS*, 309, 561, doi: [10.1046/j.1365-8711.1999.02885.x](https://doi.org/10.1046/j.1365-8711.1999.02885.x)
- . 2001, *MNRAS*, 326, 1367, doi: [10.1111/j.1365-2966.2001.04698.x](https://doi.org/10.1111/j.1365-2966.2001.04698.x)

APPENDIX

A. DATA REDUCTION

IXPE (Weisskopf et al. 2022) observed 4U 1630–47 for ~ 141 ksec between 2023 March 10 19:21:04 UTC and 2023 March 13 19:02:48 UTC under observation ID 02250601. The *IXPE* processed level-2 data was obtained from the HEASARC archive. The data are publically available from the web-site <https://heasarc.gsfc.nasa.gov/docs/ixpe/archive/>. The analysis of the *IXPE* data was performed using the IXPEOBSSIM software version 28.4.0 (Baldini et al. 2022) based on the level-2 processed data. The source region was chosen in SAOImage DS9 software (Joye & Mandel 2003) as a circular area with a $60''$ radius centered at ($16^{\text{h}}34^{\text{m}}03^{\text{s}}.3$, $-47^{\circ}23'16''.8$). We did not extract the background due to possible contamination of source photons (Di Marco et al. 2023). The PD and PA were computed using the PCUBE algorithm incorporated in IXPEOBSSIM to calculate the polarization signature of the observation independent of a model. Version 11 of the *IXPE* response functions were used to process the data.

NICER (Gendreau et al. 2012) is a soft X-ray spectral-timing instrument covering the 0.2–12 keV energy band. NICER observed the source from 2023 March 10 18:09:24 UTC to March 13 19:35:58 UTC under observation IDs 6557010XXX (101,102,201,202,301,302) for a total of ~ 32.81 ks of useful time among the 6 observations. The data were reduced using NICERDAS v10 software and the xti20221001 release of NICER CALDB products. The SCORPEON background model was adopted. Observations were filtered for hot detectors, corrected for detector deadtime, and screened to remove candidate good-time intervals with substantially elevated background or candidate intervals less than 100 s long. In the paper we show the NICER spectra combined according to Period 1 or Period 2 of the *IXPE* observation. We have used `addspect` tool from the HEASOFT package (Nasa High Energy Astrophysics Science Archive Research Center (Heasarc) 2014) for this purpose.

The *NuSTAR* (Harrison et al. 2013) spacecraft observed the source under observation IDs 8090231300#(2,4,6) and collected a total of ~ 28.35 ks of net exposure. The data were processed with the NuSTARDAS software (version 2.1.2) of the HEASOFT package (version 6.31.1). The source events were selected with a circular region of $60''$ radii centered at the source coordinates ($16^{\text{h}}34^{\text{m}}01^{\text{s}}.6101$, $-47^{\circ}23'34''.806$) for both focal plane modules (FPMA/FPMB). The background region was selected as circular region with radius $\sim 91.6''$ centered at ($16^{\text{h}}34^{\text{m}}46^{\text{s}}.6422$, $-47^{\circ}24'03''.752$). The first observation was taken during the Period 1 with lower flux, while the other two observations correspond to the Period 2. We compared the spectra and combined the 2nd and 3rd spectra for each FPM using `addspect` from FTOOL to have one representative spectra per FPM for the Period 2.

B. SPECTRAL FIT

In order to study the polarization properties of the thermal and Comptonized component we performed a joint fit on the NICER and *NuSTAR* spectra of the SPL state observation. Since our aim here is only to give an estimate of the polarization degree and angle of the two spectral components, we performed our analysis on the two instruments' time-averaged spectra, subdivided into two groups each, corresponding to Periods 1 and 2 of the SPL state *IXPE* observation. Moreover, to further simplify our approach, we restricted our study to the 2–10 keV energy range for NICER data and to the 8–70 keV range for *NuSTAR* ones in order to reduce cross-calibration uncertainties between the two instruments. The choice to analyze *NuSTAR* data starting from 8 keV, in particular, belongs to the large inconsistencies between the NICER and *NuSTAR* data below this energy—although some cross-calibration residuals can still be observed in the 8–9 keV range. We used the *NuSTAR* spectra up to 70 keV since above that the background was comparable to the data. A complete, time-resolved spectral analysis, as well as the study of the low energy inconsistencies between NICER and *NuSTAR* data, is beyond the scope of this paper and will be addressed in a future publication. We used the XSPEC package (v12.13.0c) and employed the following model in the analysis:

$$\text{edge} * \text{edge} * \text{tbabs}(\text{kerrbb} + \text{nthcomp}). \quad (\text{B1})$$

The model comprises of thermal thin accretion disk emission accounting for relativistic effects (`kerrbb`, Li et al. 2005), thermally Comptonized continuum emission (`nthcomp`, Zdziarski et al. 1996; Życki et al. 1999), and absorption by the interstellar medium (`tbabs`, Wilms et al. 2000). Following the approach from Paper I, we fixed the distance of the source in the `kerrbb` model to the value of $D = 11.5$ kpc; moreover, we kept the system inclination fixed at the value of $i = 75^{\circ}$, leaving only the black hole spin, mass, and accretion rate free to vary in the fitting procedure. A `cloudy`

(Ferland et al. 2017) absorption table was used in Paper I to model the absorption lines detected in the observation of the source in HSS, likely produced by a highly-ionized outflowing plasma (i.e. with ionization parameter $\xi \approx 10^5$ and hydrogen column density $N_H \approx 10^{24} \text{ cm}^{-2}$). If we use the `cloudy` component and assume the same ionization parameter of the HSS observation, it is possible to obtain an upper limit of $N_H \leq 10^{22} \text{ cm}^{-2}$ on the wind column density along the line of sight. However, if the ionization parameter is allowed to vary freely it is usually fitted to unrealistically high values. Additionally, the SPL state observation shows no prominent absorption lines so this component was no longer used in the fitting procedure. We used the `nthcomp` component assuming either disk blackbody or blackbody seed radiation. For Fit 1, we assumed multicolor disk blackbody seed radiation (`inp_type` parameter = 1) and fixed its temperature to the values obtained from initial modeling using `diskbb` ($kT_{\text{bb}} = 1.46^{+0.02}_{-0.01}$, $1.54^{+0.01}_{-0.02}$ keV in Period 1 and 2, respectively). For Fit 2, we used a single blackbody as the input radiation (`inp_type` parameter = 0) and instead left the temperature free to vary in the fitting procedure. The `nthcomp` input radiation modified the fluxes contributions, as presented in Table 1, and consequently the polarization properties of the power-law component. This is due to the different low energy contributions of `nthcomp` when using a multicolor black body in place of a single black body, which influences the `kerrbb` accretion rate in the fitting procedure and consequently the thermal radiation contribution to the total flux. Figure 6 shows the unfolded spectra and data residuals for both fits. The Period 2 `kerrbb` contribution to the total flux in Fit 2 is significantly larger than in Fit 1 as denoted by the dashed green lines.

Additionally, following Paper I, an empirical absorption `edge` model was used at 2.42 and 9.51 keV to account for reported instrumental features in the NICER and *NuSTAR* spectra, respectively (Wang et al. 2021; Podgorny et al. 2023). The cross-calibration model MBPO employed in Krawczynski et al. (2022) was used to account for cross-calibration uncertainties between NICER and *NuSTAR* allowing the spectral slope and normalization to vary. For the *NuSTAR* focal plane module A (FPMA) we fixed the normalization to 1 for all fitting groups, corresponding to the recommended value in Madsen et al. (2022) and kept the slope fixed to zero. For the fit presented in Table 2 we obtained the normalization values of 1.035 ± 0.002 and 0.994 ± 0.001 , and the slope values of 0.0664 ± 0.0033 and 0.0095 ± 0.0025 , for the NICER and *NuSTAR* FPMB observations, respectively. The best-fit parameters of this analysis are shown in Table 2 for a $\chi^2/\text{dof} = 2502.68/2399$, when using a disk blackbody input radiation for the `nthcomp` component, and a $\chi^2/\text{dof} = 2470.75/2399$ assuming a blackbody input for the power-law component. It is worth noting that in our simplified approach the data are consistently above the model in the high energy tail of the spectra (45–70 keV) with both models further motivating the need for a more detailed analysis of the spectral properties of this source.

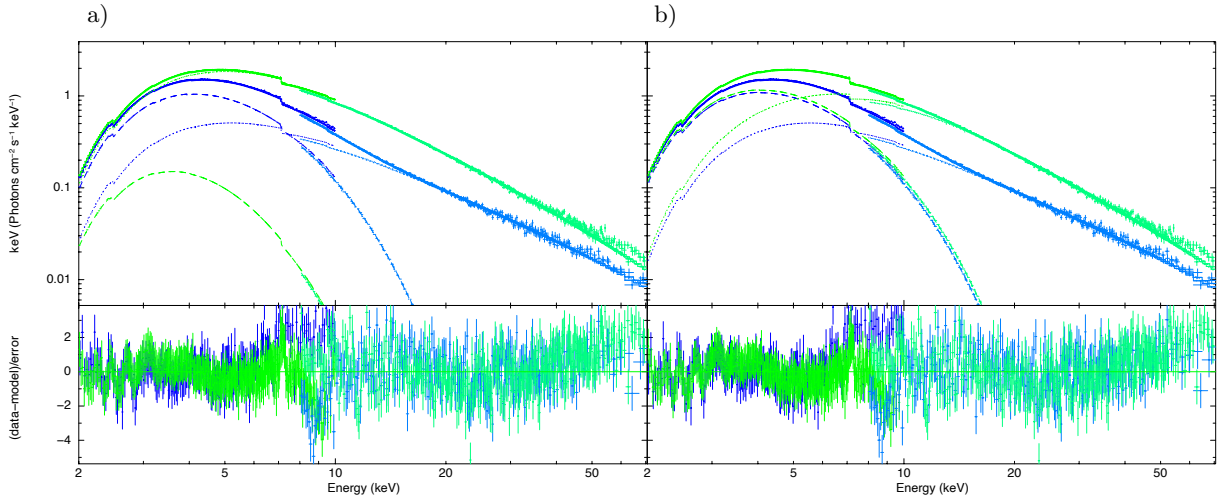


Figure 6. Fits of 4U 1630–47 NICER and *NuSTAR* X-ray spectra for Period 1 (blue) and Period 2 (green): a) Disk blackbody assumed as seed radiation for the power-law component (Fit 1). b) Single temperature blackbody assumed as seed radiation for the power-law component (Fit 2). Unfolded spectra around the best-fitting model in F_E representation, the total model (solid) and the `kerrbb` (dashed) and `nthcomp` (dotted) contributions for each data set are shown in the top panels while the data-model residuals in σ are shown in the bottom panels.

Table 2. Spectral fit parameters

Component	Parameter (unit)	Description	Value Fit 1		Value Fit 2	
			SPL Period 1	SPL Period 2	SPL Period 1	SPL Period 2
tbabs	N_{H} (10^{22} cm^{-2})	Hydrogen column density	$7.84^{+0.02}_{-0.04}$	$7.71^{+0.02}_{-0.02}$	$7.63^{+0.03}_{-0.03}$	$7.78^{+0.02}_{-0.02}$
kerrbb	η	Disk power ratio	0 (frozen)	-	-	-
	a	Black hole spin	$0.71^{+0.25}_{-0.15}$	-	$0.72^{+0.18}_{-0.21}$	-
	i (deg)	Inclination	75.00 (frozen)	-	-	-
	M_{bh} (M_{\odot})	Black hole mass	$10.51^{+3.51}_{-2.54}$	-	$9.37^{+2.95}_{-2.14}$	-
	M_{dd} (10^{18} g s^{-1})	Effective mass accretion rate	$6.22^{+0.98}_{-0.33}$	$1.22^{+0.25}_{-0.21}$	$4.91^{+0.61}_{-0.48}$	$6.91^{+0.57}_{-0.61e}$
	D (kpc)	Distance	11.5 (frozen)	-	-	-
	hd	Hardening factor	1.7 (frozen)	-	-	-
	r_{flag}	Self-irradiation	1 (frozen)	-	-	-
	l_{flag}	Limb-darkening	0 (frozen)	-	-	-
	norm	norm	Normalization	1.0 (frozen)	-	-
nthcomp	Γ	Photon index	$2.64^{+0.02}_{-0.01}$	$2.94^{+0.01}_{-0.01}$	$2.61^{+0.02}_{-0.02}$	$2.93^{+0.01}_{-0.01}$
	kT_e (keV)	Electron temperature	500.00 (frozen)	-	-	-
	kT_{bb} (keV)	Seed photon temperature	$1.46^{+0.02}_{-0.01}$	$1.54^{+0.01}_{-0.02}$	$0.91^{+0.24}_{-0.18}$	$1.88^{+0.38}_{-0.36}$
	inp_type	Seed photon shape	1.0 (frozen)	-	0.0 (frozen)	-
	z	Redshift	0.0 (frozen)	-	-	-
	norm	norm	Normalization	$1.09^{+0.02}_{-0.02}$	$3.68^{+0.01}_{-0.01}$	$0.41^{+0.05}_{-0.05}$
edge 1	edgeE (keV)	Threshold energy	$2.43^{+0.01}_{-0.01}$	-	-	-
	MaxTau (10^{-2})	Absorption Depth at threshold energy	$6.14^{+0.40}_{-0.41}$	-	-	-
edge 2	edgeE (keV)	Threshold energy	$9.49^{+0.05}_{-0.05}$	-	-	-
	MaxTau (10^{-2})	Absorption Depth at threshold energy	$1.88^{+0.21}_{-0.22}$	-	-	-

NOTE—Best-fitting parameters for joint NICER and *NuSTAR* spectral fitting for periods corresponding to Period 1 and Period 2. Uncertainties are stated at the 90% confidence level. Parameters are calculated assuming a disk blackbody seed radiation (Fit 1) or a blackbody seed radiation (Fit 2) for the power-law component of the spectra.

As a following step, we included *IXPE* spectra in the fitting procedure, dividing them into two groups corresponding to the periods of the SPL state observation. We allowed all the parameters of the MBPO model to vary independently for each of the three *IXPE* detector units in both periods. For the fits presented in Table 2, we found the $\Delta\Gamma_1$ values of 0.118 ± 0.033 , 0.073 ± 0.032 , 0.099 ± 0.019 , the $\Delta\Gamma_2$ values of -0.27 ± 0.11 , -0.41 ± 0.19 , -0.77 ± 0.31 , the E_{br} values of 4.43 ± 0.38 , 4.79 ± 0.45 , 5.46 ± 0.34 and the normalization values of 0.7361 ± 0.0046 , 0.7036 ± 0.0054 , 0.6786 ± 0.0049 for the *IXPE* DUs 1,2,3, respectively, in Period 1 of the SPL state. In Period 2, we obtained the following values for the three *IXPE* DUs: $\Delta\Gamma_1 = 0.013 \pm 0.011$, 0.075 ± 0.018 , 0.076 ± 0.016 ; $\Delta\Gamma_2 = 0.59 \pm 0.15$, -0.416 ± 0.063 , 0.458 ± 0.097 ; $E_{\text{br}} = 5.47 \pm 0.25$, 4.64 ± 0.20 , 5.00 ± 0.26 ; normalization of 0.7204 ± 0.0042 , 0.7184 ± 0.0033 , 0.6843 ± 0.0029 . We found that the best-fitting model has a $\chi^2/\text{dof} = 3693.90/3293$. The reduced χ^2 is greater than one even accounting for 1% systematic uncertainties for the NICER data sets, within the mission’s recommendations² This result is likely due to our simplified approach of performing a time-averaged analysis on a highly variable source.

² NICER calibration recommendations can be found at https://heasarc.gsfc.nasa.gov/docs/nicer/analysis_threads/cal-recommend/.